

Superconducting triplet pairing in Al/Al₂O₃/Ni/Ga junctions

Andreas Costa,^{1,*} Madison Sutula,^{2,3} Valeria Lauter,⁴ Jia Song,² Jaroslav Fabian,^{1,†} and Jagadeesh S. Moodera^{2,5,‡}

¹*Institute for Theoretical Physics, University of Regensburg, 93040 Regensburg, Germany*

²*Francis Bitter Magnet Laboratory and Plasma Science and Fusion Center,
Massachusetts Institute of Technology, MA 02139, USA*

³*Department of Materials Science and Engineering, Massachusetts Institute of Technology, MA 02139, USA*

⁴*Neutron Scattering Division, Neutron Sciences Directorate,
Oak Ridge National Laboratory, Oak Ridge, TN 37831, USA*

⁵*Department of Physics, Massachusetts Institute of Technology, MA 02139, USA*

(Dated: August 17, 2024)

Ni/Ga bilayers are a versatile playground for exploring the competition of the strongly antagonistic ferromagnetic and superconducting phases. Systematically characterizing this competition's impact on highly ballistic Al/Al₂O₃/Ni/Ga junctions' transport properties from both the experimental and theoretical viewpoints, we identify novel conductance peak structures, which are caused by superconducting triplet pairings at the Ni/Ga interface, and which are widely adjustable through the Ni–Ga thickness ratio. We demonstrate that these conductance anomalies persist even in the presence of an in-plane magnetic field, which provides—together with the detection of the paramagnetic Meissner effect in Ga—the clear experimental evidence that the observed conductance features serve indeed as the triplet pairings' unique transport fingerprints. Our work demonstrates that Ni/Ga bilayers have a strong potential for superconducting spintronics applications, in particular for triplet-pairing engineering.

Introduction. Magnetic superconducting junctions form elementary building blocks for superconducting spintronics [1–5], with potential applications in quantum computing [6–13]. Early conductance measurements on ferromagnet/superconductor point contacts [14, 15] demonstrated that Andreev reflection can be used to quantify the ferromagnet's spin polarization [16]. Nowadays, more complex structures, such as magnetic Josephson-junction geometries [17], in which Yu–Shiba–Rusinov states [18–20] can strongly influence the supercurrent [21, 22] and even induce current-reversing $0\text{-}\pi$ transitions [23, 24], are being exploited. A wealth of unique physical phenomena and transport anomalies has been predicted to emerge in such junctions, covering the potential formation of Majorana states [25–33], significantly magnified current magnetoanisotropies [34–37], as well as the efficient generation and detection of spin-polarized triplet Cooper pair currents [3, 38].

Particularly appealing materials for superconducting spintronics are Ni/Ga (Bi) bilayers [39, 40], as strong proximity effects turn the intrinsically weakly ferromagnetic Ni film superconducting. The coexistence of the two nominally antagonistic ferromagnetic and superconducting phases within the Ni region might strongly modify transport properties such as the differential conductance. Most remarkable is the possibility to generate spin-triplet states, as previous studies [38, 41–58] concluded that ferromagnetic exchange can induce odd-frequency superconductivity as a signature of triplet pairing.

The two main factors that generate triplet pairing in proximitized s -wave superconductors are noncollinearly magnetized domains and spin-orbit coupling effects. While triplet currents originating from noncollinear magnetizations were successfully implemented in various systems [43, 47, 48, 59–67]—e.g., in Nb/Py/Co/Py/Nb junctions through tilting the thin permalloy (Py) spin-mixers' magnetizations [66]—generating them through spin-orbit coupling [52, 53] is more challenging

and often requires specific magnetization configurations (with respect to the spin-orbit field) to induce detectable triplet pairings [68–71].

In this Letter, we systematically investigate the conductance of high-quality superconducting magnetic Al/Al₂O₃/Ni/Ga junctions and demonstrate, in combination with realistic theoretical simulations, the generation of triplet pairings due to the presence of Ni/Ga bilayers. Specifically, we observe unexpected conductance peak structures, which strongly depend on the Ni–Ga film-thickness ratio. This ratio controls the effective spin-orbit coupling's strength at the Ni/Ga interface, and provides an extremely efficient knob to adjust the triplet pairing. An applied in-plane magnetic field does not significantly influence the conductance spectra, which is a clear evidence that the superconducting triplet pairings dominate these peculiar features. Furthermore, we detect the paramagnetic Meissner effect in Ga, which is yet another key evidence for the presence of an odd-frequency superconducting triplet state [50, 72–74]. We believe that our findings pave the way for employing Ni/Ga-based magnetic superconducting tunnel junctions as platforms for investigating outstanding superconducting phenomena, such as Majorana states [25–33], magnetoanisotropies [34–37], or triplet supercurrents [3, 38], in a controllable way.

Experimental and theoretical methods. All investigated junctions, with cross-section areas of $150\text{ }\mu\text{m} \times 150\text{ }\mu\text{m}$, were prepared by means of thermal evaporation inside an UHV system with a base pressure of 2×10^{-8} mb, using in-situ shadow-masking techniques. During the growth process, thin films of Al, Ni, and Ga were evaporated on clean glass slides at roughly 80 K. The junctions' ultrathin Al₂O₃ barriers, separating adjacent Al and Ni/Ga films, were likewise created in situ through exposing Al to controlled oxygen plasma. Before taking the junctions out of the UHV chamber, they were protected by 10 nm thick Al₂O₃ layers. In one run,

we could thereby prepare 72 junctions with different Ni and Ga film thicknesses (keeping all other growth parameters the same), allowing us to study the Ni and Ga films' individual impact on the junctions' transport characteristics in a well-controllable manner. To perform the tunneling conductance measurements, we attached 24 distinct junctions to a probe with electrical leads and immersed the system into a pumped liquid-helium bath to achieve temperatures below 1 K. Both the Al and Ni/Ga thin films turned superconducting, with critical temperatures (and superconducting gaps) strongly depending on their thicknesses [75]. For instance, we deduced a critical temperature of about 2.5 K for a 4 nm Al film, whereas the Ni/Ga bilayer's critical temperature varied from about 4 K to 7 K (thicker Ni leads to lower critical temperature). Apart from becoming superconducting through proximity, Meservey–Tedrow spectroscopy [76–78] indicated weak ferromagnetic exchange inside the Ni film (i.e., spin polarization below 1 %, notably increasing above 4 nm Ni thickness). The subsequently presented tunneling conductance *vs.* junction bias data was obtained using standard lock-in technique.

To unravel the conductance anomalies' physical origin, we compare the experimental outcomes against theoretical simulations. For the latter, we discretize the Al/Ni/Ga junctions on a two-dimensional tight-binding grid and compute the tunneling density of states (DOS) [75], which can be directly mapped to the taken conductance data, within the python transport package KWANT [79]. The aforementioned Al₂O₃ barriers, and also EuS spacers present in some samples [80, 81]—that can significantly enhance triplet-pair currents further [82, 83]—are not expected to be relevant to characterize the experimental results and not part of our theoretical modeling. As reference parameters, we take the constant number of lattice sites $L_{\text{Al}} = 200$ inside the Al region (mimicking 4 nm thick Al), as well as Ga's zero-temperature superconducting gap $|\Delta_{\text{S,Ga}}(0)| = 1.358$ meV that we experimentally estimated from one specific sample; all remaining material parameters [i.e., “thicknesses” L_{Ni} and L_{Ga} , and gaps $|\Delta_{\text{S,Al}}(0)|$ and $|\Delta_{\text{S,Ni}}(0)|$] are then rescaled following their experimental values [75].

Ferromagnetic-exchange effects. Summarizing our rich tunneling conductance–bias voltage data, tuning the individual films' thicknesses allows for a universal switching between different transport regimes.

As long as the outer Ga region is thick enough (semi-infinite in theory), all the junctions' conductance characteristics are fully describable within the earlier established Octavio–Tinkham–Blonder–Klapwijk modeling [84–86], essentially resulting in the formation of a well-distinct subharmonic conductance gap structure with less pronounced peaks at voltages $V \approx \pm 2|\Delta_{\text{S,Al}}(0)|/(2ne)$, and more marked ones at $V \approx \pm|\Delta_{\text{S,Ga}}(0)|/e$ and $V \approx \pm[|\Delta_{\text{S,Al}}(0)| + |\Delta_{\text{S,Ga}}(0)|]/e$; e denotes the positive elementary charge and n a positive integer. The intermediate Ni film's superconducting gap does not have a great impact owing to the largely extended Ga electrode (whose gap is moreover nearly five times larger than Ni's). As we show in the Supplementary [75], we can ex-

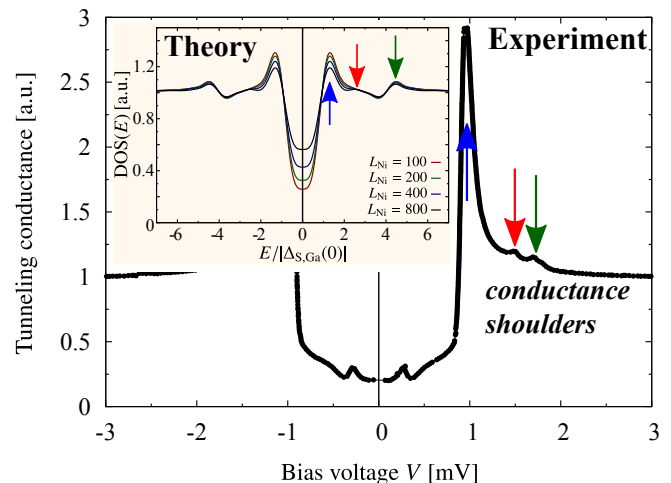


FIG. 1. *Measured* tunneling conductance–bias voltage characteristics of Al (4 nm)/Al₂O₃ (0.4 nm)/EuS (1.4 nm)/Ni (0.8 nm)/Ga (20 nm) junctions at 1.07 K. *INSET:* *Calculated* zero-temperature tunneling DOS as a function of particle energy E and for different indicated numbers of lattice sites (“thicknesses”) L_{Ni} of weakly ferromagnetic Ni; $L_{\text{Al}}/L_{\text{Ga}} = 200/1000 = (4 \text{ nm})/(20 \text{ nm})$ is kept constant. Colored arrows highlight qualitatively reproducible conductance (DOS) peaks (shoulders).

perimentally recover this regime in junctions containing about 60 nm Ga.

Decreasing Ga's thickness leads to an intricate interplay between *all* materials' superconducting gaps and Ni's ferromagnetic exchange splitting, notably altering the junctions' conductance features. As an example, Fig. 1 displays Al (4 nm)/Al₂O₃ (0.4 nm)/EuS (1.4 nm)/Ni (0.8 nm)/Ga (20 nm) junctions' tunneling conductance–voltage characteristics. Most surprisingly, we witness a subseries of *weak local conductance maxima* (called “conductance shoulders”) in addition to the still present (sharp) conductance peak(s). Since such conductance shoulders have not yet been addressed in earlier works, we support the experiment with numerical KWANT simulations of the junctions' zero-temperature tunneling DOS—noting that the transport anomalies are microscopically caused by the formation of resonant Andreev bound states [87, 88] that we can likewise identify as DOS peaks.

Already thin Ni films raise a pronounced DOS peak at $eV \approx |\Delta_{\text{S,Ga}}(0)|$, followed by a much weaker “DOS shoulder”, whose position is now determined by *all* superconducting gaps (as opposed to the case in which Ga extends to infinity). Although these DOS peaks' positions do quantitatively not exactly coincide with the experiment (due to simplifications in the model), the related conductance peaks are *qualitatively* clearly resolvable in the experimental measurements. The second conductance shoulder experimentally observed in between the two computed DOS peaks must be ascribed to an additional peak splitting triggered by Ni's exchange coupling. Since we substituted a rather small Ni spin polarization of less than 0.1 % into the DOS simulations—demonstrating that weak ferro-

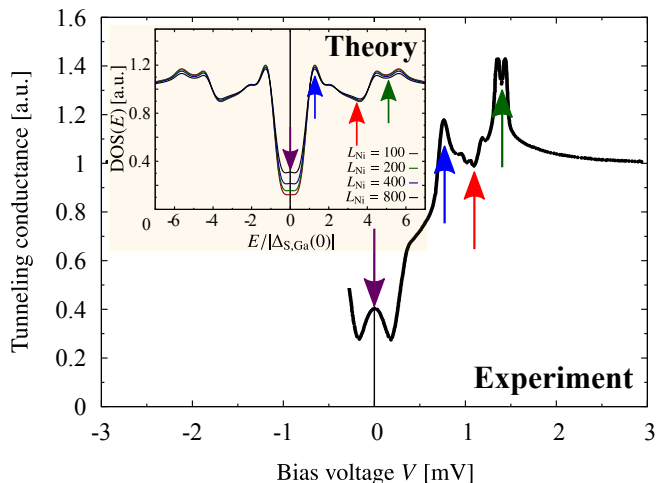


FIG. 2. *Measured* tunneling conductance–bias voltage characteristics of Al (4 nm)/Al₂O₃ (0.4 nm)/Ni (1.6 nm)/Ga (30 nm) junctions at 1.2 K. *INSET*: *Calculated* zero-temperature tunneling DOS—assuming *strong* superconducting triplet pairings at the Ni/Ga interface—and for different indicated numbers of lattice sites (“thicknesses”) L_{Ni} of *weakly* ferromagnetic Ni; $L_{\text{Al}}/L_{\text{Ga}} = 200/2000 = (4 \text{ nm})/(40 \text{ nm})$ is kept constant. Colored arrows highlight qualitatively reproducible conductance (DOS) peaks (shoulders).

magnetism in Ni suffices to explain the measurements—recovering the related peak splitting in the tunneling DOS requires rather large Ni thicknesses (recall that we estimated about 1 % spin polarization from the samples). As it completely disappears when turning Ni *nonferromagnetic* (even at Ni thicknesses far above Ga’s), the additionally appearing conductance shoulder must indeed originate from the interplay between Ni’s ferromagnetism and superconductivity, and serves therefore as a clear transport fingerprint of (weak) ferromagnetism inside Ni. From the microscopic viewpoint, the formation of the respective DOS shoulder might signify the intriguing competition between Andreev bound states [87, 88] and Yu–Shiba–Rusinov states [18–20] in magnetic Josephson junctions [21, 22]. The conductance peak close to zero bias is not clearly resolvable in the DOS simulations, which is probably a consequence of our simplified model (neglecting, i.e., the influence of the EuS layer present in this sample).

Signatures of triplet pairing. Further increasing the Ni–Ga thickness ratio from $d_{\text{Ni}}/d_{\text{Ga}} = 0.04$ in the previous to $d_{\text{Ni}}/d_{\text{Ga}} \approx 0.053$ in Al (4 nm)/Al₂O₃ (0.4 nm)/Ni (1.6 nm)/Ga (30 nm) junctions lets an even more puzzling competition between ferromagnetism and superconductivity occur. Each of the above identified conductance peaks (shoulders) splits into a set of subseries, finally merging into highly nontrivial tunneling conductance–bias voltage relations; see Fig. 2. Since these samples do not contain ferromagnetic EuS layers, all peak splittings are solely triggered by Ni. Interestingly, we detect a marked zero-bias conductance peak, which might be seen as a precursor of zero-energy Andreev (Yu–Shiba–

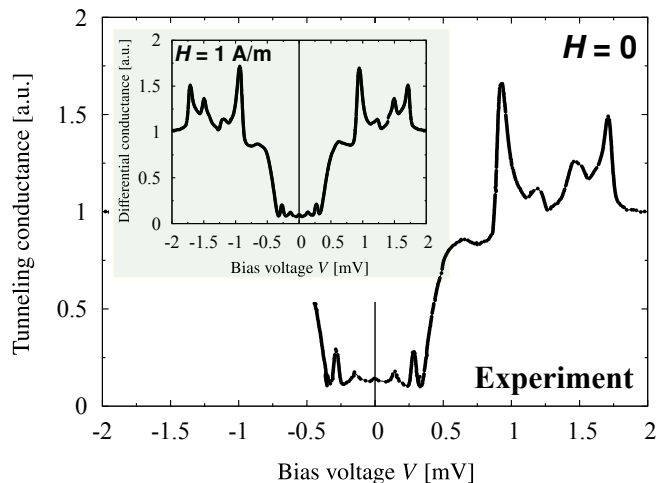


FIG. 3. *Measured* tunneling conductance–bias voltage characteristics of Al (4 nm)/Al₂O₃ (0.4 nm)/EuS (1.2 nm)/Ni (1.6 nm)/Ga (30 nm)/Al₂O₃ (12 nm) junctions at 1 K. *INSET*: *Measured* tunneling conductance–bias voltage characteristics of the same sample, measured in an in-plane magnetic field of strength $H = 1 \text{ Am}^{-1}$.

Rusinov) bound states.

Comparing the conductance modulations against our theoretical tunneling-DOS simulations, we deduce that the experimental findings are qualitatively only reproducible if we assume that not just singlet superconducting pairing is present (as up to now), but moreover *strong triplet pairings at the Ni/Ga interface* arise. To see clear effects, the triplet-pairing potentials substituted into our DOS simulations are exaggeratedly large (i.e., nearly four times larger than the singlet-pairing potentials), explaining the quantitative deviations between the DOS and conductance peaks’ (shoulders’) positions. Nickel’s spin polarization remains as tiny as before (below 0.1 %) to show that weak ferromagnetism together with strong triplet pairings replicates the conductance variations (larger ferromagnetic exchange and weaker triplet pairings act similarly).

We can exclude that the unprecedented conductance anomalies simply result from ferromagnetic proximity effects alone, which Ni induces in the adjacent Ga film (see our polarized-neutron reflectometry studies). Despite magnifying the zero-bias conductance (DOS) peak, the remaining conductance peak subseries are then not fully reproducible [75]. Therefore, the experimental measurements suggest the existence of both *interfacial triplet pairings* and *ferromagnetic proximity effects*. Analogously, introducing superconducting triplet correlations in the bulk of Ni and Ga (instead of at their interface) does also not fully cover the experimental outcomes, and would turn the zero-bias peaks into dips. As all the crucial physics must consequently happen right at the Ni/Ga interface, growing the same sample once again *interchanging the Ni and Ga films* does not visibly alter the conductance spectrum.

Let us now verify that those interface effects result in the theoretically proposed (strong) superconducting triplet pairings, exploiting that the ferromagnetic and singlet superconduct-

ing phases are strongly antagonistic. Applying sufficiently large magnetic fields to a singlet superconductor typically tends to break up its Cooper pairs and aligns all unpaired electrons' spins parallel to generate net magnetic moments. As a consequence, the superconducting order gets slowly destroyed and the associated order parameter, i.e., the singlet superconducting gap, is suppressed. Since the observed conductance peaks' positions in our study are essentially determined by the individual films' superconducting gaps, applying a magnetic field would not only reduce the gaps themselves, but concurrently visibly displace the apparent conductance peaks.

Measuring the conductance–voltage characteristics of Al (4 nm)/Al₂O₃ (0.4 nm)/EuS (1.2 nm)/Ni (1.6 nm)/Ga (30 nm)/Al₂O₃ (12 nm) junctions once in the absence and once in the presence of an external in-plane magnetic field, however, does *not* reveal any substantial impact of the magnetic field on the conductance peaks, as illustrated in Fig. 3. The striking physics, leading to the described conductance anomalies, must therefore indeed originate from interfacial triplet pairings, whose gaps are much less sensitive to external magnetic fields. The overall conductance modulations are now even richer than before (additional peak splittings), mostly due to the EuS layer whose strong ferromagnetic exchange coupling [80, 81] further amplifies the peak-splitting effects. These splittings turn the previously discussed zero-bias conductance peak into another series of closely adjacent conductance peaks.

Polarized-neutron reflectometry. To investigate the Meissner effect in Ni/Ga films and directly obtain their structure [by low-angle X-ray reflectometry (XRR) studies] and magnetization-depth profile, we employ the polarized-neutron reflectometry (PNR) method. PNR was previously successfully applied to observe the diamagnetic Meissner effect, as well as vortex-line distributions, in niobium and YBCO bilayer films [89, 90]. Here, we report the detection of the paramagnetic Meissner effect in Ga—another key property of the odd-frequency superconducting triplet state generated through the proximity coupling of the Ni/Ga bilayer. For the PNR-data analysis, we distinguish between two scenarios: the first is consistent with the conventional *diamagnetic* Meissner screening and the second corresponds to the *paramagnetic* Meissner response in Ga. The results for both cases are shown in Fig. 4(a) and 4(b). Fitting the PNR (obtained at 5 K, which is below that bilayer's superconducting critical temperature) and XRR data, we observe that the Ni (5.6 nm)/Ga (25 nm) interface is sharp with a roughness of 0.5 nm (see Figs. S5 and S6 in the Supplementary [75]). The PNR spin-asymmetry ratio $SA = (R^+ - R^-)/(R^+ + R^-)$ reveals that the best fit to the data requires 26 emu/cc induced magnetization over roughly 6 nm in Ga, while the magnetization in the Ni film is about 136 emu/cc and uniform. Thus, we are able to directly see the induced ferromagnetic order's influence inside the Ga layer right at the interface with the Ni film, which must be attributed to the paramagnetic Meissner response. PNR provides hence the expected evidence that superconducting Ni/Ga bilayers exhibit the paramagnetic Meissner response in Ga as a

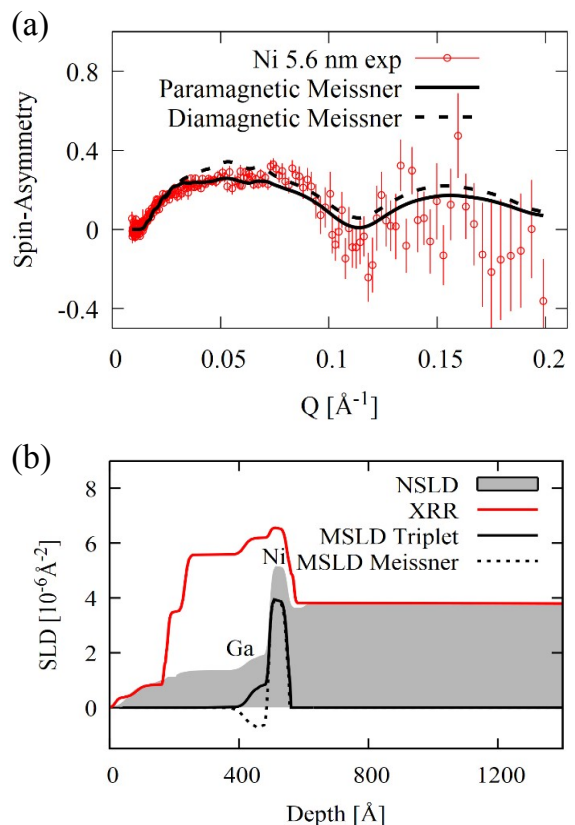


FIG. 4. Polarized-neutron reflectometry (PNR) results for Ni (5.6 nm)/Ga (25 nm) bilayer. (a) PNR spin-asymmetry ratio $SA = (R^+ - R^-)/(R^+ + R^-)$; the best fit to the data corresponds to the magnetization profile shown as the solid black line in (b)—paramagnetic Meissner state—, revealing 26 emu/cc induced magnetization over about 6 nm in Ga, while the Ni film's magnetization is about 136 emu/cc and uniform. Contrary, the diamagnetic Meissner state in the spin-asymmetry (SA) plot and its magnetic scattering length density (MSLD) profile, referring to the dashed black lines, strongly deviate from the experimental data.

clear signature of the theoretically predicted superconducting triplet state [50, 72–74].

Conclusions. We demonstrated that the coexistence of the nominally opposing ferromagnetic and superconducting phases in Ni/Ga bilayers gives rise to intriguing modulations of Al/Al₂O₃/Ni/Ga junctions' tunneling conductance–bias voltage relations, which are essentially controlled by the Ni–Ga film-thickness ratio and can be reproduced in a well-defined manner in several distinct junctions. Mapping theoretical tunneling-DOS simulations to the experimental conductance data, we predicted that large enough Ni–Ga thickness ratios support sizable superconducting triplet pairings at the Ni/Ga interface, most likely stemming from interfacial spin-orbit couplings. To further characterize the specific triplet-pairing mechanism, we suggest to subsequently focus more on the junctions' Josephson-transport characteristics.

Acknowledgments. The experimental work performed in the U.S. was supported by the NSF Grant DMR 1700137, ONR Grants N00014-16-1-2657 and N00014-20-1-2306, and John Templeton Foundation Grants 39944 and 60148. The theoretical work at Regensburg (A.C. and J.F.) received funding from the Elite Network of Bavaria through the International Doctorate Program Topological Insulators and Deutsche Forschungsgemeinschaft (DFG, German Research Foundation)—Project-ID 314695032—SFB 1277, Subproject B07. The undergraduate M.S. was supported by the UROP program funds at Massachusetts Institute of Technology. This research used resources at the Spallation Neutron Source, a DOE Office of Science User Facility operated by the Oak Ridge National Laboratory.

* E-Mail: andreas.costa@physik.uni-regensburg.de

† E-Mail: jaroslav.fabian@physik.uni-regensburg.de

‡ E-Mail: moodera@mit.edu

- [1] I. Žutić, J. Fabian, and S. Das Sarma, *Rev. Mod. Phys.* **76**, 323 (2004).
- [2] J. Fabian, A. Matos-Abiague, C. Ertler, P. Stano, and I. Žutić, *Acta Phys. Slovaca* **57**, 565 (2007).
- [3] M. Eschrig, *Phys. Today* **64**, 43 (2011).
- [4] J. Linder and J. W. A. Robinson, *Sci. Rep.* **5**, 15483 (2015).
- [5] K. Ohnishi, S. Komori, G. Yang, K.-R. Jeon, L. A. B. Olde Olthof, X. Montiel, M. G. Blamire, and J. W. A. Robinson, *Appl. Phys. Lett.* **116**, 130501 (2020).
- [6] L. B. Ioffe, V. B. Geshkenbein, M. V. Feigel'man, A. L. Fauchère, and G. Blatter, *Nature* **398**, 679 (1999).
- [7] J. E. Mooij, T. P. Orlando, L. Levitov, L. Tian, C. H. van der Wal, and S. Lloyd, *Science* **285**, 1036 (1999).
- [8] G. Blatter, V. B. Geshkenbein, and L. B. Ioffe, *Phys. Rev. B* **63**, 174511 (2001).
- [9] A. V. Ustinov and V. K. Kaplunenko, *J. Appl. Phys.* **94**, 5405 (2003).
- [10] T. Yamashita, K. Tanikawa, S. Takahashi, and S. Maekawa, *Phys. Rev. Lett.* **95**, 097001 (2005).
- [11] A. K. Feofanov, V. A. Oboznov, V. V. Bol'ginov, J. Lisenfeld, S. Poletto, V. V. Ryazanov, A. N. Rossolenko, M. Khabipov, D. Balashov, A. B. Zorin, P. N. Dmitriev, V. P. Koshelets, and A. V. Ustinov, *Nat. Phys.* **6**, 593 (2010).
- [12] M. I. Khabipov, D. V. Balashov, F. Maibaum, A. B. Zorin, V. A. Oboznov, V. V. Bolginov, A. N. Rossolenko, and V. V. Ryazanov, *Supercond. Sci. Technol.* **23**, 045032 (2010).
- [13] M. H. Devoret and R. J. Schoelkopf, *Science* **339**, 1169 (2013).
- [14] R. J. Soulen Jr., *Science* (80-.) **282**, 85 (1998).
- [15] R. J. Soulen Jr., M. S. Osofsky, B. Nadgorny, T. Ambrose, P. Broussard, S. F. Cheng, J. Byers, C. T. Tanaka, J. Nowack, J. S. Moodera, G. Laprade, A. Barry, and M. D. Coey, *J. Appl. Phys.* **85**, 4589 (1999).
- [16] M. J. M. de Jong and C. W. J. Beenakker, *Phys. Rev. Lett.* **74**, 1657 (1995).
- [17] A. A. Golubov, M. Y. Kupriyanov, and E. Il'ichev, *Rev. Mod. Phys.* **76**, 411 (2004).
- [18] L. Yu, *Acta Phys. Sin.* **21**, 75 (1965).
- [19] H. Shiba, *Prog. Theor. Phys.* **40**, 435 (1968).
- [20] A. I. Rusinov, *Zh. Eksp. Teor. Fiz. Pisma Red.* **9**, 146 (1968); *JETP Lett.* **9**, 85 (1969).
- [21] A. Costa, J. Fabian, and D. Kochan, *Phys. Rev. B* **98**, 134511 (2018).
- [22] D. Kochan, M. Barth, A. Costa, K. Richter, and J. Fabian, *Phys. Rev. Lett.* **125**, 087001 (2020).
- [23] L. N. Bulaevskii, V. V. Kuzii, and A. A. Sobyanin, *Pis'ma Zh. Eksp. Teor. Fiz.* **25**, 314 (1977); *JETP Lett.* **25**, 290 (1977).
- [24] V. V. Ryazanov, V. A. Oboznov, A. Y. Rusanov, A. V. Veretennikov, A. A. Golubov, and J. Aarts, *Phys. Rev. Lett.* **86**, 2427 (2001).
- [25] J. Nilsson, A. R. Akhmerov, and C. W. J. Beenakker, *Phys. Rev. Lett.* **101**, 120403 (2008).
- [26] M. Duckheim and P. W. Brouwer, *Phys. Rev. B* **83**, 054513 (2011).
- [27] S.-P. Lee, J. Alicea, and G. Refael, *Phys. Rev. Lett.* **109**, 126403 (2012).
- [28] S. Nadj-Perge, I. K. Drozdov, J. Li, H. Chen, S. Jeon, J. Seo, A. H. MacDonald, B. A. Bernevig, and A. Yazdani, *Science* **346**, 602 (2014).
- [29] E. Dumitrescu, B. Roberts, S. Tewari, J. D. Sau, and S. Das Sarma, *Phys. Rev. B* **91**, 094505 (2015).
- [30] R. Pawlak, M. Kisiel, J. Klinovaja, T. Meier, S. Kawai, T. Glatzel, D. Loss, and E. Meyer, *npj Quantum Inf.* **2**, 16035 (2016).
- [31] M. Ruby, B. W. Heinrich, Y. Peng, F. von Oppen, and K. J. Franke, *Nano Lett.* **17**, 4473 (2017).
- [32] G. Livanas, M. Sigrist, and G. Varelogiannis, *Sci. Rep.* **9**, 6259 (2019).
- [33] S. Manna, P. Wei, Y. Xie, K. T. Law, P. A. Lee, and J. S. Moodera, *Proc. Natl. Acad. Sci.* **117**, 8775 (2020).
- [34] P. Högl, A. Matos-Abiague, I. Žutić, and J. Fabian, *Phys. Rev. Lett.* **115**, 116601 (2015); *Phys. Rev. Lett.* **115**, 159902(E) (2015).
- [35] S. H. Jacobsen, I. Kulagina, and J. Linder, *Sci. Rep.* **6**, 23926 (2016).
- [36] A. Costa, P. Högl, and J. Fabian, *Phys. Rev. B* **95**, 024514 (2017).
- [37] I. Martínez, P. Högl, C. González-Ruano, J. P. Cascales, C. Tiusan, Y. Lu, M. Hehn, A. Matos-Abiague, J. Fabian, I. Žutić, and F. G. Aliev, *Phys. Rev. Appl.* **13**, 014030 (2020), 1812.08090.
- [38] R. S. Keizer, S. T. B. Goennenwein, T. M. Klapwijk, G. Miao, G. Xiao, and A. Gupta, *Nature* **439**, 825 (2006).
- [39] J. S. Moodera and R. Meservey, *Phys. Rev. B* **42**, 179 (1990).
- [40] P. LeClair, J. S. Moodera, J. Philip, and D. Heiman, *Phys. Rev. Lett.* **94**, 037006 (2005).
- [41] W. Belzig, C. Bruder, and G. Schön, *Phys. Rev. B* **53**, 5727 (1996).
- [42] A. Kadigrobov, R. I. Shekhter, and M. Jonson, *Europhys. Lett.* **54**, 394 (2001).
- [43] F. S. Bergeret, A. F. Volkov, and K. B. Efetov, *Phys. Rev. Lett.* **86**, 4096 (2001).
- [44] F. S. Bergeret, A. F. Volkov, and K. B. Efetov, *Rev. Mod. Phys.* **77**, 1321 (2005).
- [45] T. Yokoyama, Y. Tanaka, and A. A. Golubov, *Phys. Rev. B* **75**, 134510 (2007).
- [46] J. Linder, T. Yokoyama, A. Sudbø, and M. Eschrig, *Phys. Rev. Lett.* **102**, 107008 (2009).
- [47] T. S. Khaire, M. A. Khasawneh, W. P. Pratt Jr., and N. O. Birge, *Phys. Rev. Lett.* **104**, 137002 (2010).
- [48] J. W. A. Robinson, J. D. S. Witt, and M. G. Blamire, *Science* **329**, 59 (2010).
- [49] M. S. Anwar, F. Czeschka, M. Hesselberth, M. Porcu, and J. Aarts, *Phys. Rev. B* **82**, 100501(R) (2010).
- [50] T. Yokoyama, Y. Tanaka, and N. Nagaosa, *Phys. Rev. Lett.* **106**, 246601 (2011).

- [51] F. S. Bergeret, A. Verso, and A. F. Volkov, *Phys. Rev. B* **86**, 060506(R) (2012).
- [52] F. S. Bergeret and I. V. Tokatly, *Phys. Rev. Lett.* **110**, 117003 (2013).
- [53] F. S. Bergeret and I. V. Tokatly, *Phys. Rev. B* **89**, 134517 (2014).
- [54] A. Di Bernardo, S. Diesch, Y. Gu, J. Linder, G. Divitini, C. Ducati, E. Scheer, M. G. Blamire, and J. W. A. Robinson, *Nat. Commun.* **6**, 8053 (2015).
- [55] J. Arjoranta and T. T. Heikkilä, *Phys. Rev. B* **93**, 024522 (2016).
- [56] C. Espedal, T. Yokoyama, and J. Linder, *Phys. Rev. Lett.* **116**, 127002 (2016).
- [57] A. Pal, J. A. Ouassou, M. Eschrig, J. Linder, and M. G. Blamire, *Sci. Rep.* **7**, 3 (2017).
- [58] F. S. Bergeret and I. V. Tokatly, *Phys. Rev. B* **102**, 060506(R) (2020).
- [59] F. S. Bergeret, A. F. Volkov, and K. B. Efetov, *Phys. Rev. Lett.* **86**, 3140 (2001).
- [60] F. S. Bergeret, A. F. Volkov, and K. B. Efetov, *Phys. Rev. B* **64**, 134506 (2001).
- [61] M. Eschrig, J. Kopu, J. C. Cuevas, and G. Schön, *Phys. Rev. Lett.* **90**, 137003 (2003).
- [62] M. Houzet and A. I. Buzdin, *Phys. Rev. B* **76**, 060504(R) (2007).
- [63] M. Eschrig and T. Löfwander, *Nat. Phys.* **4**, 138 (2008).
- [64] R. Grein, M. Eschrig, G. Metalidis, and G. Schön, *Phys. Rev. Lett.* **102**, 227005 (2009).
- [65] J. W. A. Robinson, G. B. Halász, A. I. Buzdin, and M. G. Blamire, *Phys. Rev. Lett.* **104**, 207001 (2010).
- [66] N. Banerjee, J. W. A. Robinson, and M. G. Blamire, *Nat. Commun.* **5**, 1 (2014).
- [67] S. Diesch, P. Machon, M. Wolz, C. Sürgers, D. Beckmann, W. Belzig, and E. Scheer, *Nat. Commun.* **9**, 5248 (2018).
- [68] N. Satchell and N. O. Birge, *Phys. Rev. B* **97**, 214509 (2018).
- [69] N. Satchell, R. Loloee, and N. O. Birge, *Phys. Rev. B* **99**, 174519 (2019).
- [70] J. R. Eskilt, M. Amundsen, N. Banerjee, and J. Linder, *Phys. Rev. B* **100**, 224519 (2019).
- [71] B. Bujnowski, R. Biele, and F. S. Bergeret, *Phys. Rev. B* **100**, 224518 (2019).
- [72] K. Machida and R. A. Klemm, *Solid State Commun.* **27**, 1061 (1978).
- [73] Y. Asano, Y. V. Fominov, and Y. Tanaka, *Phys. Rev. B* **90**, 094512 (2014).
- [74] A. Di Bernardo, Z. Salman, X. L. Wang, M. Amado, M. Egilmez, M. G. Flokstra, A. Suter, S. L. Lee, J. H. Zhao, T. Prokscha, E. Morenzoni, M. G. Blamire, J. Linder, and J. W. A. Robinson, *Phys. Rev. X* **5**, 041021 (2015).
- [75] See the attached Supplemental Material, including Refs. [76–79, 84–87, 89, 91–95], for more details.
- [76] P. M. Tedrow and R. Meservey, *Phys. Rev. Lett.* **26**, 192 (1971).
- [77] P. M. Tedrow and R. Meservey, *Phys. Rev. B* **7**, 318 (1973).
- [78] R. Meservey and P. M. Tedrow, *Phys. Rep.* **238**, 173 (1994).
- [79] C. W. Groth, M. Wimmer, A. R. Akhmerov, and X. Waintal, *New J. Phys.* **16**, 063065 (2014).
- [80] J. S. Moodera, X. Hao, G. A. Gibson, and R. Meservey, *Phys. Rev. Lett.* **61**, 637 (1988).
- [81] E. Strambini, V. N. Golovach, G. De Simoni, J. S. Moodera, F. S. Bergeret, and F. Giazotto, *Phys. Rev. Mater.* **1**, 054402 (2017).
- [82] G. De Simoni, E. Strambini, J. S. Moodera, F. S. Bergeret, and F. Giazotto, *Nano Lett.* **18**, 6369 (2018).
- [83] M. Rouco, S. Chakraborty, F. Aikebaier, V. N. Golovach, E. Strambini, J. S. Moodera, F. Giazotto, T. T. Heikkilä, and F. S. Bergeret, *Phys. Rev. B* **100**, 184501 (2019).
- [84] J. M. Rowell and W. L. Feldmann, *Phys. Rev.* **172**, 393 (1968).
- [85] M. Octavio, M. Tinkham, G. E. Blonder, and T. M. Klapwijk, *Phys. Rev. B* **27**, 6739 (1983).
- [86] K. Flensberg, J. Bindslev Hansen, and M. Octavio, *Phys. Rev. B* **38**, 8707 (1988).
- [87] A. F. Andreev, *Zh. Eksp. Teor. Fiz.* **46**, 1823 (1964); *J. Exp. Theor. Phys.* **19**, 1228 (1964).
- [88] A. F. Andreev, *Zh. Eksp. Teor. Fiz.* **49**, 655 (1966); *J. Exp. Theor. Phys.* **22**, 455 (1966).
- [89] V. Lauter-Pasyuk, H. J. Lauter, V. L. Aksenov, E. I. Kornilov, A. V. Petrenko, and P. Leiderer, *Physica B* **248**, 166 (1998).
- [90] V. Lauter-Pasyuk, H. J. Lauter, M. Lorenz, V. L. Aksenov, and P. Leiderer, *Physica B* **267-268**, 149 (1999).
- [91] G. B. Arnold, *J. Low Temp. Phys.* **59**, 143 (1985).
- [92] G. B. Arnold, *J. Low Temp. Phys.* **68**, 1 (1987).
- [93] Y. M. Blanter and F. W. J. Hekking, *Phys. Rev. B* **69**, 024525 (2004).
- [94] M. Kuhlmann, U. Zimmermann, D. Dikin, S. Abens, K. Keck, and V. M. Dmitriev, *Z. Phys. B* **96**, 13 (1994).
- [95] V. Lauter-Pasyuk, *Collect. Soc. Fr. Neutron* **7**, s221 (2007).

SUPPLEMENTAL MATERIAL

Superconducting triplet pairing in Al/Al₂O₃/Ni/Ga junctions

Andreas Costa,^{1,*} Madison Sutula,^{2,3} Valeria Lauter,⁴ Jia Song,² Jaroslav Fabian,^{1,†} and Jagadeesh S. Moodera^{2,5,‡}

¹*Institute for Theoretical Physics, University of Regensburg, 93040 Regensburg, Germany*

²*Francis Bitter Magnet Laboratory and Plasma Science and Fusion Center, Massachusetts Institute of Technology, MA 02139, USA*

³*Department of Materials Science and Engineering, Massachusetts Institute of Technology, MA 02139, USA*

⁴*Neutron Scattering Division, Neutron Sciences Directorate, Oak Ridge National Laboratory, Oak Ridge, TN 37831, USA*

⁵*Department of Physics, Massachusetts Institute of Technology, MA 02139, USA*

In this Supplemental Material, we introduce two distinct theoretical approaches applied to understand the experimentally investigated Al/Al₂O₃/Ni/Ga junctions' puzzling tunneling conductance–voltage characteristics. Section I summarizes the individual layers' most essential material parameters that were extracted from (some of) the prepared samples and enter our theoretical simulations as a fundamental input. In Sec. II, we adapt the well-established analytical Octavio–Tinkham–Blonder–Klapwijk (OTBK) model [S1, S2] to cover these junctions and extract some valuable general conductance features, which are able to partially explain the experimental results. Afterwards, we outline the greatest drawbacks of the OTBK description in view of our systems and elaborate on more sophisticated numerical simulations, employing the python tight-binding transport code KWANT [S3], in Sec. III. Section IV clarifies the influence of likewise present ferromagnetic proximity effects on the discussed outcomes, before we eventually analyze additional polarized-neutron reflectometry data in Sec. V to provide a deeper insight into the magnetization profile at the Ni/Ga interface.

CONTENTS

I. Junction parameters	i
II. Analytical OTBK calculations vs. experimental measurements	ii
III. Numerical KWANT simulations—generic recipe	iv
IV. Role of purely ferromagnetic proximity effects	vi
V. Polarized-neutron reflectometry	vii
References	viii

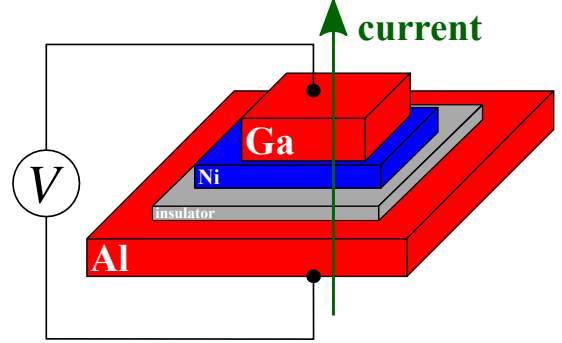


FIG. S1. Schematic sketch of the investigated Al/insulator (i.e., Al₂O₃)/Ni/Ga junctions. The Al and Ga electrodes are intrinsically superconducting, while proximity effects additionally turn the weakly ferromagnetic Ni film likewise superconducting. Applying the bias voltage V between the electrodes and measuring the related tunneling current (indicated by the dark green arrow), we probe the samples' tunneling conductance–bias voltage characteristics.

I. JUNCTION PARAMETERS

As we stated in the main text, Al/Al₂O₃/Ni/Ga junctions (see Fig. S1 for a schematic sketch) offer unprecedented possibilities to investigate the intriguing interplay of the nominally antagonistic ferromagnetic and superconducting states of matter. Apart from the already intrinsically superconducting Al and Ga components, proximity effects turn also the weakly ferromagnetic Ni film additionally superconducting. The individual layers' (zero-temperature) superconducting energy gaps and critical temperatures vary usually a lot with the distinct films' thicknesses. We extracted their values from (some of) the experimental samples. For junctions built on 4 nm Al, the latter's critical temperature was estimated to be $T_{C,Al} = 2.5$ K, whereas that of the Ni/Ga bilayer typically drops down with increasing Ni thickness, reaching $T_{C,Ni} = T_{C,Ga} = 4.2$ K for about 2 nm thin Ni. For simplicity, we use the same critical temperatures everywhere along the Ni/Ga bilayer (also in the potentially present interfacial Ni–Ga alloy right at the Ni/Ga boundary). The Ni/Ga bilayer's (zero-temperature) superconducting energy gaps were quantified in one sample containing a 2.4 nm Ni interlayer, while the gap of Al remains roughly the same as its bulk value. All these parameters provide the essential input for our theoretical simulations that we

* E-Mail: andreas.costa@physik.uni-regensburg.de

† E-Mail: jaroslav.fabian@physik.uni-regensburg.de

‡ E-Mail: moodera@mit.edu

TABLE S1. Material parameters estimated from (some of) the experimental samples and used for our theoretical simulations.

Al electrode	zero-temperature superconducting gap	$ \Delta_{S,Al}(0) = 0.18 \text{ meV}$
	critical temperature	$T_{C,Al} = 2.5 \text{ K}$
Ni film	zero-temperature superconducting gap	$ \Delta_{S,Ni}(0) = 0.277 \text{ meV}$
	critical temperature	$T_{C,Ni} = 4.2 \text{ K}$
NiGa interfacial alloy	zero-temperature superconducting gap	$ \Delta_{S,NiGa}(0) = 0.251 \text{ meV}$
	critical temperature	$T_{C,NiGa} = 4.2 \text{ K}$
Ga electrode	zero-temperature superconducting gap	$ \Delta_{S,Ga}(0) = 1.358 \text{ meV}$
	critical temperature	$T_{C,Ga} = 4.2 \text{ K}$

will discuss in the following, and are summarized in a compact way in Tab. S1.

The Ni region truly counts to the most crucial components of the junctions, as it does not only turn superconducting through proximity effects, but shows additionally weak intrinsic ferromagnetism, and might hence raise clear spin-polarized transport features. Its spin polarization, which we classified by means of state-of-the-art Meservey–Tedrow spectroscopy [S4–S6], rises with increasing Ni film thickness. For instance, samples with about 4 nm thick Ni revealed spin polarizations slightly below one percent.

II. ANALYTICAL OTBK CALCULATIONS VS. EXPERIMENTAL MEASUREMENTS

To theoretically access Al/Al₂O₃/Ni/Ga junctions’ generic tunneling conductance–bias voltage characteristics and compare them against the experimental data, we apply two distinct methods. The first approach essentially generalizes the earlier established Octavio–Tinkham–Blonder–Klapwijk (OTBK) modeling [S1, S2] to a simple toy system that captures all essential parts of the experimental samples. More specifically, we idealize the junctions in terms of effective *one-dimensional* Al/N/Ni/NiGa/Ga point contacts, whose thin nonsuperconducting normal-metal link (N) of thickness d gets separated by two strong ultrathin (deltalike) barriers from the neighboring Al and Ni regions to resemble the samples’ Al₂O₃ tunneling barriers. Following earlier works, we calculate the overall tunneling-current flow (and thereby the tunneling conductance) in the same manner as explained in Refs. [S1] and [S2], taking the material parameters summarized in Tab. S1. The perhaps greatest strength of the OTBK approach is that we can reliably control all single junction parameters and deduce their resolved impact on the whole junctions’ conductance characteristics. Since experimental observations suggested that the Ni/Ga bilayers may additionally form thin Ni–Ga alloys at their interfaces, our model also accounts for the latter (though they are extremely thin and their gap is thus small that they do not visibly impact the calculated conductances).

Figures S2(A)–(C) illustrate the numerically evaluated tunneling conductance–bias voltage relations of *symmetric* Ga/N/Ni/NiGa/Ga junctions (meaning that we are concerned with two *similar* massive Ga electrodes), held at a temperature of 0.5 K. The thickness of the intermediate Ni film gets gradually increased from $d_{Ni} = 0.5 \text{ nm}$ to $d_{Ni} = 2.0 \text{ nm}$, and finally to $d_{Ni} = 5.0 \text{ nm}$, while we consider the Ni spin polarization $P_{Ni} = 1 \%$; recall that Meservey–Tedrow spectroscopy on the experimental samples concluded Ni spin polarizations below one percent. For the (deltalike) tunneling barriers that separate the normal-state region (N) from the Ga and Ni layers, and basically resemble the samples’ Al₂O₃ tunneling barriers, we assume realistic barrier heights of 0.75 eV together with thicknesses of about 0.80 nm, coinciding with experiment.

As long as the Ni region remains thin enough, we recover S/N/S junctions’ unique subharmonic conductance gap structure [S1, S2], manifesting itself in pronounced conductance maxima at all bias voltages $V \approx 2|\Delta_{S,Ga}(0)|/(ne)$ with integer n (e denotes the positive elementary charge). The physical origin of that subharmonic gap structure is analyzed in Refs. [S7] and [S8]. Multiple Andreev reflections [S9] of incident electrons (holes) at the N/Ga and N/Ni interfaces, respectively, open additional transmission channels through which unpaired electrons (strictly speaking, electronlike quasiparticles) can tunnel from one into the second Ga electrode. Only at bias voltages fulfilling $V \approx 2|\Delta_{S,Ga}(0)|/(ne)$, these tunnelings involve large-density of states (DOS) states to become likely enough to raise *sizable* tunneling current contributions; the latter become eventually visible in terms of local maxima in the junctions’ conductance–voltage characteristics. Nevertheless, we need to account for another peculiarity of Andreev reflections in *magnetic* junctions. Each electron (hole) approaching the N/Ni boundary and being Andreev reflected picks up the extra phase $\delta\phi = (\Delta_{XC,Ni}d_{Ni})/(\hbar v_{F,Ni})$ [S10], where $\Delta_{XC,Ni}$ (d_{Ni}) indicates Ni’s exchange splitting (thickness) and $v_{F,Ni}$ its Fermi velocity. Since Andreev reflections are strongly phase sensitive, additional phases of incident electrons (holes) may notably change the probabilities to really undergo Andreev reflections. For certain values of $\delta\phi$, it might even become possible that Andreev reflections become suddenly forbidden at their initially favored

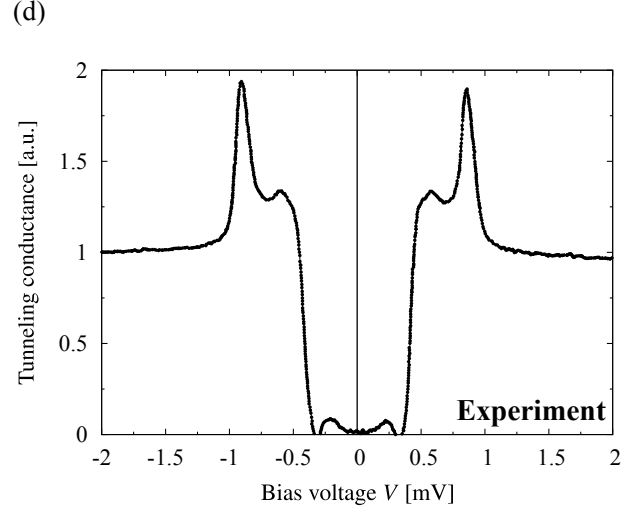
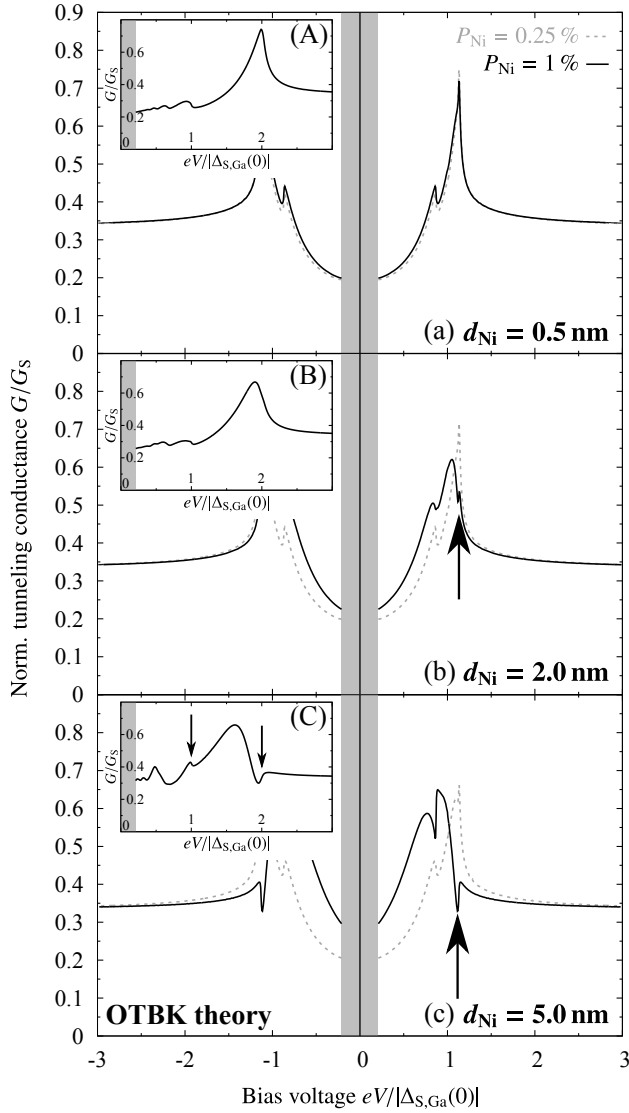


FIG. S2. (a)–(c) *Calculated* dependence of Al/N/Ni/NiGa/Ga junctions’ tunneling conductance G , normalized to Sharvin’s conductance G_S , on the applied bias voltage V [the associated electron energy eV is given in multiples of Ga’s zero-temperature superconducting gap $|\Delta_{S,\text{Ga}}(0)|$] for two indicated Ni spin polarizations P_{Ni} and Ni thicknesses (a) $d_{\text{Ni}} = 0.5$ nm, (b) $d_{\text{Ni}} = 2.0$ nm, and (c) $d_{\text{Ni}} = 5.0$ nm at 0.5 K. (d) *Measured* tunneling conductance–voltage characteristics of one specific Al (4 nm)/Al₂O₃ (0.4 nm)/Ni (3 nm)/Ga (60 nm) junction at 0.58 K. (A)–(C) Same as in (a)–(c), but for *symmetric* Ga/N/Ni/NiGa/Ga junctions. Black arrows highlight *anomalous conductance variations*, i.e., increasing Ni thicknesses may turn conductance maxima into minima. At small voltages, the tunneling current becomes tiny and calculating its values accurately enough is numerically demanding; we shaded this region and do not present any data there.

bias voltages $V \approx 2|\Delta_{S,\text{Ga}}(0)|/(ne)$, and happen then primarily at voltages well below or above. As a consequence, the conductance-enhancing electron tunnelings are no longer possible at $V \approx 2|\Delta_{S,\text{Ga}}(0)|/(ne)$, turning prior conductance maxima into conductance dips and simultaneously raising new maxima at other voltages. The full effect is predominantly controllable by means of $\delta\phi$ and thus by altering either $\Delta_{\text{XC},\text{Ni}}$ or d_{Ni} . In our simulations, we observe such clear modifications when increasing d_{Ni} from $d_{\text{Ni}} = 2.0$ nm to $d_{\text{Ni}} = 5.0$ nm, keeping $\Delta_{\text{XC},\text{Ni}}$ (essentially its spin polarization P_{Ni}) constant. The initially arising conductance maximum at $eV \approx 2|\Delta_{S,\text{Ga}}(0)|$ really turns into a conductance minimum (dip), as the additionally accumulated $\delta\phi$ heavily suppresses conductance-

enhancing multiple Andreev reflections there.

Coming back to the experimentally studied junctions, we replace the left Ga electrode by Al and repeat the same theoretical calculations, now distinguishing between the two Ni spin polarizations $P_{\text{Ni}} = 0.25\%$ and $P_{\text{Ni}} = 1\%$; see Figs. S2(a)–(c). It is important to recognize that Ga’s (zero-temperature) superconducting gap is more than seven times as large as that of Al. Rowell and Feldman [S1, S11] deduced that such dramatic imbalances between *dissimilar* electrodes’ superconducting gaps strongly alter the subharmonic gap structure and split the series of conductance maxima into well-distinct subseries. Transferring those results to our case, we expect local conductance peaks forming at $eV \approx \pm 2|\Delta_{S,\text{Al}}(0)|/(2n)$ with pos-

itive integers n , $eV \approx \pm|\Delta_{S,\text{Ga}}(0)|$, and $eV \approx \pm[|\Delta_{S,\text{Al}}(0)| + |\Delta_{S,\text{Ga}}(0)|]$ —at least as long as the ferromagnetic exchange in Ni can be neglected (i.e., at sufficiently small $\Delta_{\text{XC},\text{Ni}}$ and/or d_{Ni}). The latter two peaks can be clearly identified in Fig. S2(a)—though they are both located at slightly smaller voltages than expected due to the superconducting gaps’ rescaling at finite temperatures. The peak subseries originating from Al, however, cannot be properly resolved since the tunneling current becomes thus tiny at small bias voltages that calculating its values within the required accuracy would be demanding. For that reason, we shaded this area in the plots and do not present any numerical data there. The interfacial Ni–Ga alloy has no visible influence on the outcomes, as it is assumed to be ultrathin (0.6 nm) and its superconducting gap is again much smaller than that of the neighboring Ga electrode. Increasing the thickness of Ni or its spin polarization (exchange splitting) acts similarly as above. The additional phases the Andreev-reflected electrons (holes) accumulate start to play a major role and can significantly change the conductance peaks’ positions. Large enough phases (at large enough Ni thicknesses and/or spin polarizations) flatten the conductance peaks and may even split them into further subseries [see Figs. S2(b)–(c)].

Comparing our calculations presented in Figs. S2(a)–(c) to the experimental conductance data obtained for Al (4 nm)/Al₂O₃ (0.4 nm)/Ni (3 nm)/Ga (60 nm) junctions at 0.58 K [see Fig. S2(d)] confirms that the Ni spin polarization extracted from Meservy–Tedrow spectroscopy (less than one percent) is a reasonable value. The Ni thickness of the experimental sample, $d_{\text{Ni}} = 3$ nm, lies quite close to the theoretical case shown in Fig. S2(b), for which we considered $d_{\text{Ni}} = 2$ nm. Regarding the qualitative conductance–voltage dependence, the experimental data matches quite well the theoretical curve indicating $P_{\text{Ni}} = 1\%$ except that the additional peak splitting at $eV \approx \pm|\Delta_{S,\text{Ga}}(0)|$ could not be experimentally observed, suggesting that Ni’s spin polarization in the sample must indeed be smaller than one percent. Nevertheless, we cannot quantitatively fit our model to the experimental data since the junction parameters given in Tab. S1 were only determined for some samples and are not precisely known for all of them. The experimental results in Fig. S2(d) indeed reveal (slightly) different superconducting gaps than those we substituted into our calculations. The reduction to one-dimensional junctions is another issue our theory might face. Earlier studies [S12] demonstrated that the tunneling-current flow through three-dimensional junctions is not homogeneous (e.g., due to inhomogeneities in the oxide barriers) and rather carried by different transverse channels. Each channel could be subject to distinct interfacial scattering (barrier) parameters, additionally shifting the conductance peaks and explaining deviations between theory and experiment. Extending our model to three dimensions and accounting for different transverse momentum-dependent barrier parameters is feasible, but goes beyond the scope of this work. At the moment, it is sufficient to understand that Al/Al₂O₃/Ni/Ga junctions’ peculiar tunneling conductance–voltage characteristics are predominantly governed by the interplay between the strongly

differing superconducting gaps of the Al and Ga electrodes on the one, and Ni’s ferromagnetic exchange interaction on the other hand.

III. NUMERICAL KWANT SIMULATIONS— GENERIC RECIPE

Most surprisingly, the bias voltages at which conductance maxima arise in Figs. S2(a)–(c) are not visibly influenced by Ni’s superconducting gap, although we claimed that proximity effects turn Ni superconducting and an unprecedented competition with its intrinsic ferromagnetic properties might occur. The main reason for that illustrates another great deficit of the OTBK formulation. Since this approach regards the junctions’ Al and Ga regions as massive, infinitely extended, electrodes, the superconducting gap of the much thinner Ni layer—simultaneously being several times tinier than Ga’s gap—will not have a substantial impact on the calculated conductance peak positions. Even enhancing Ni’s superconducting gap *within a reasonable range* would not lead to significant changes of the obtained conductance data.

The experimental results depicted in Fig. S2(d) were recorded for a sample whose 60 nm thick Ga region indeed remarkably overcomes the Ni layer’s thickness of just about 3 nm, and can hence be treated to some extent like a semi-infinite Ga electrode. This observation justifies the good agreement between the OTBK modeling’s theoretical predictions and the experimental outcomes for that particular junction configuration. Nevertheless, as soon as the Ga electrode becomes much thinner and the Ni layer gains more importance in determining the samples’ overall transport characteristics, the OTBK description might face serious trouble and we can no longer compare those calculations with the experimental outcomes. As this is essentially the case with all junctions analyzed in the main text, we urgently need to elaborate on a second and more powerful method that can efficiently model electrical transport through more realistic physical systems and notably extends our analytical possibilities.

For that purpose, we implement the experimentally studied Al/Ni/Ga stackings within the python transport package KWANT [S3], basically discretizing their continuous Bogoljubov–de Gennes Hamiltonian on a discrete tight-binding lattice. For simplicity, we consider a two-dimensional square lattice with spacing $a = 1$ [a.u.] between two adjacent lattice sites; each site with the real-space coordinates $(z, y) = (ai, aj)$ is then uniquely identified by its integer lattice “coordinates” (i, j) . Figure S3(a) shows a graphical representation of the chosen tight-binding lattice. We denote the numbers of lattice sites along the longitudinal \hat{z} -direction inside the Al, Ni, and Ga junction regions by L_{Al} , L_{Ni} , and L_{Ga} , respectively, whereas we assume in total W lattice sites along the transverse \hat{y} -direction. Contrary to the aforementioned OTBK modeling, we do *not* include the Al₂O₃ tunneling barriers and the interfacial Ni–Ga alloy into our KWANT description since we are predominantly interested in deducing qualitative trends, which would not be dramatically affected by those two components.

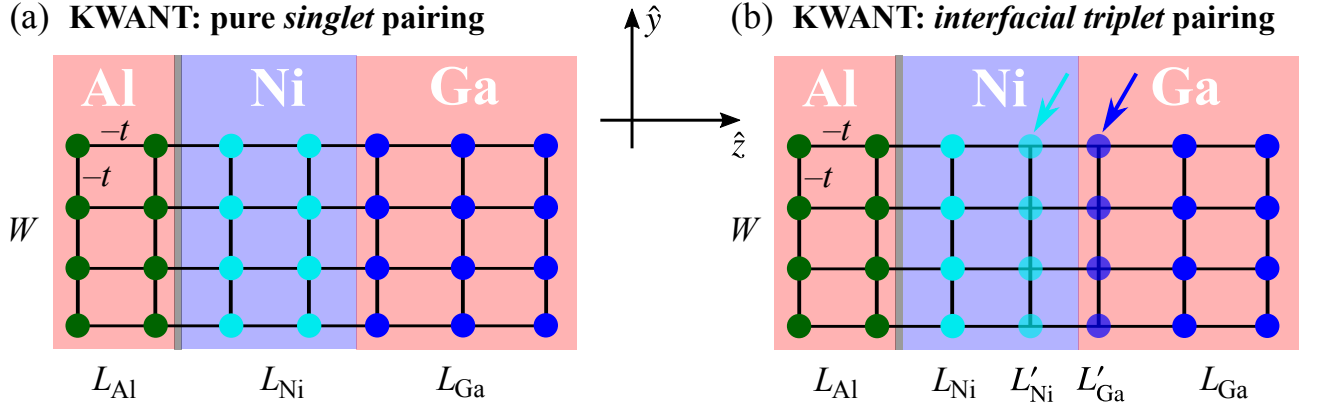


FIG. S3. (a) Schematic illustration of Al/Ni/Ga junctions' *tight-binding modeling* within the KWANT python transport package, starting from a square lattice with constant spacing $a = 1$ [a.u.]. The numbers of horizontal lattice sites inside the junctions' different regions are denoted by L_{Al} , L_{Ni} , and L_{Ga} , respectively, and that along the transverse direction by W . Colored dots represent the *on-site energies*, determined by the Bogoljubov–de Gennes Hamiltonian stated in Eq. (S1), while t measures the strength of the *nearest-neighbor hoppings*. All superconducting pairing potentials capture only pure singlet pairings. (b) Same as in (a), but assuming that the superconducting pairing potentials in the Ni and Ga layers combine singlet with *interfacial triplet* pairings [within the lattice sites $(L'_{\text{Ni}}; L'_{\text{Ga}})$]; the latter are emphasized by colored arrows.

The *on-site energies* at lattice site (i, j) are then given by the discretized Nambu-space Bogoljubov–de Gennes Hamiltonian

$$\begin{aligned}
 \hat{\mathcal{H}}_{\text{BdG}}(i, j) = & \left[(4t - \mu) \hat{\tau}_0 \right. \\
 & + |\Delta_{\text{S,Al}}^{\text{singlet}}| \hat{\tau}_2 \Theta(i) \Theta(L_{\text{Al}} - i) \\
 & + \Delta_{\text{XC,Ni}} \hat{\tau}_1 \Theta(i - L_{\text{Al}} - 1) \Theta(L_{\text{Al}} + L_{\text{Ni}} + L'_{\text{Ni}} - i) \\
 & + |\Delta_{\text{S,Ni}}^{\text{singlet}}| \hat{\tau}_2 \Theta(i - L_{\text{Al}} - 1) \Theta(L_{\text{Al}} + L_{\text{Ni}} + L'_{\text{Ni}} - i) \\
 & + |\Delta_{\text{S,Ni}}^{\text{triplet}}| \hat{\tau}_3 \Theta(i - L_{\text{Al}} - L_{\text{Ni}} - 1) \Theta(L_{\text{Al}} + L_{\text{Ni}} + L'_{\text{Ni}} - i) \\
 & + |\Delta_{\text{S,Ga}}^{\text{singlet}}| \hat{\tau}_2 \Theta(i - L_{\text{Al}} - L_{\text{Ni}} - L'_{\text{Ni}} - 1) \Theta(L_{\text{Al}} + L_{\text{Ni}} + L'_{\text{Ni}} + L'_{\text{Ga}} + L_{\text{Ga}} - i) \\
 & \left. + |\Delta_{\text{S,Ga}}^{\text{triplet}}| \hat{\tau}_3 \Theta(i - L_{\text{Al}} - L_{\text{Ni}} - L'_{\text{Ni}} - 1) \Theta(L_{\text{Al}} + L_{\text{Ni}} + L'_{\text{Ni}} + L'_{\text{Ga}} - i) \right] \\
 & \times \Theta(j) \Theta(W - 1 - j)
 \end{aligned} \tag{S1}$$

and the *nearest-neighbor hoppings* ($\langle i, j \rangle$ indicates nearest-neighbor lattice sites) by

$$\hat{\mathcal{H}}_{\text{hop}}(\langle i, j \rangle) = -t \hat{\tau}_0, \tag{S2}$$

where

$$\hat{\tau}_0 = \begin{bmatrix} 1 & 0 & 0 & 0 \\ 0 & 1 & 0 & 0 \\ 0 & 0 & -1 & 0 \\ 0 & 0 & 0 & -1 \end{bmatrix}, \quad \hat{\tau}_1 = \begin{bmatrix} 1 & 0 & 0 & 0 \\ 0 & -1 & 0 & 0 \\ 0 & 0 & 1 & 0 \\ 0 & 0 & 0 & -1 \end{bmatrix}, \quad \hat{\tau}_2 = \begin{bmatrix} 0 & 0 & 1 & 0 \\ 0 & 0 & 0 & 1 \\ 1 & 0 & 0 & 0 \\ 0 & 1 & 0 & 0 \end{bmatrix}, \quad \text{and} \quad \hat{\tau}_3 = \begin{bmatrix} 0 & 0 & 0 & 1 \\ 0 & 0 & 1 & 0 \\ 0 & 1 & 0 & 0 \\ 1 & 0 & 0 & 0 \end{bmatrix}. \tag{S3}$$

Thereby, the hopping parameter represents $t = \hbar^2/(2ma^2)$ — m refers to the effective quasiparticle masses—, noting that it is most convenient to use such units that $a = t =$

1 [a.u.], at least as long as one focuses rather on qualitative than on quantitative analyses.

Apart from the discrete single-particle energies $\varepsilon(i, j) =$

$(4t - \mu)\hat{\tau}_0$, measured with respect to the chemical potential μ (taken to be the same throughout the junction), and Ni's ferromagnetic exchange gap $\Delta_{XC,Ni}$ (the magnetization vector points along the \hat{z} -direction), we need to account for the junction regions' distinct superconducting pairing potentials (gaps). Within the OTBK approach, all superconducting pairing potentials are simply approximated by steplike *singlet* (*s*-wave) functions. However, analyzing our numerical simulations and comparing them against the experimental results convinces that pure singlet pairings alone are not yet sufficient to reproduce all observed conductance features. Some of the samples instead reveal clear indications of additionally present *triplet pairings at the Ni/Ga interface*, which might result as a consequence of strong spin-orbit interactions due to the structure-inversion asymmetry. Covering both singlet and triplet correlations, the Bogoljubov–de Gennes Hamiltonian contains not only singlet superconducting pairing potentials, coupling spin-up and spin-down electrons to form *spin-singlet Cooper pairs*, but also triplet-pairing potentials that facilitate *spin-triplet Cooper pairs* consisting of two equal-spin electrons. The corresponding *singlet* superconducting gaps are abbreviated by $|\Delta_{S,Al}^{\text{singlet}}|$, $|\Delta_{S,Ni}^{\text{singlet}}|$, and $|\Delta_{S,Ga}^{\text{singlet}}|$, while the *interfacial triplet* gaps are $|\Delta_{S,Ni}^{\text{triplet}}|$ and $|\Delta_{S,Ga}^{\text{triplet}}|$. To ensure that triplet correlations arise indeed solely in the vicinity of the Ni/Ga interface, their respective pairing potential terms are *nonzero only* in $L'_{Ni} = L_{Ni}/5$ and $L'_{Ga} = L_{Ga}/5$ of Ni's and Ga's lattice sites around their interface (which might be seen as the previously mentioned Ni–Ga alloy region), as we schematically illustrate in Fig. S3(b). Limiting the triplet correlations to

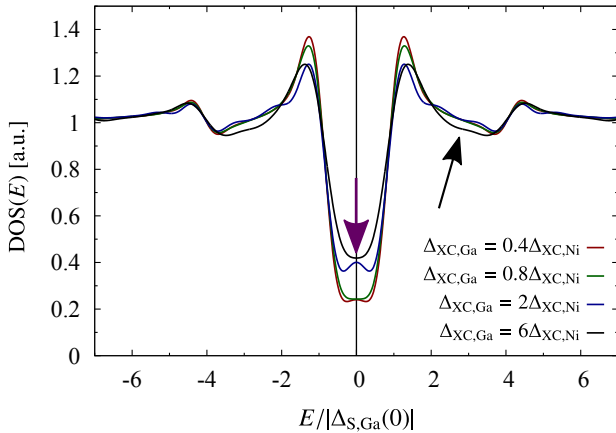


FIG. S4. Calculated zero-temperature tunneling DOS for different indicated proximity-induced exchange splittings $\Delta_{XC,Ga}$ in $1/5$ of Ga's lattice sites around the Ni/Ga interface; Ni is weakly ferromagnetic (i.e., $\Delta_{XC,Ni} = 0.5|\Delta_{S,Ga}(0)|$) corresponds to a spin polarization of less than 0.03 % and contains $L_{Ni} = 400$ lattice sites (resembling a thickness of 8 nm). All other parameters are the same as in Fig. 1 of the main text, i.e., also *no* triplet superconducting gaps are assumed to be present. Ferromagnetic proximity effects can partially cause more clearly pronounced zero-bias conductance peaks (emphasized by the violet arrow), but are not yet sufficient to reproduce all the experimentally observed conductance peak splittings at larger voltages (black arrow) that we attributed to interfacial triplet pairings in the main text.

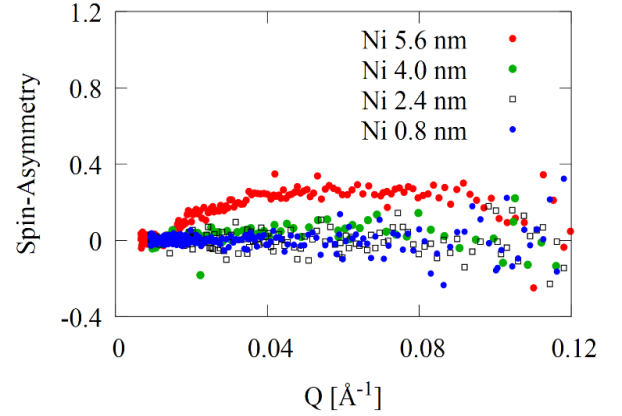


FIG. S5. Polarized-neutron spin-asymmetry ratio $SA = (R^+ - R^-)/(R^+ + R^-)$ for Ni/Ga bilayers with various Ni thicknesses.

this particular range is not motivated by the experiment, which could not satisfactorily characterize all the physics happening at the Ni/Ga boundary so far, but rather an *ad-hoc* assumption to recover the generic trends visible in the recorded conductance data. Moreover, we could not yet specify the *orbital* symmetry of the triplet-pairing potential (e.g., *p*-wave) from the current measurements.

To obtain the theoretical results discussed in the main text, we implement the aforementioned tight-binding Bogoljubov–de Gennes Hamiltonian in KWANT and use KWANT's internal Kernel Polynomial Method (KPM) to extract the junctions' spatially integrated zero-temperature tunneling DOS (normalized to its normal-state counterpart), which gets essentially probed by conductance measurements and is therefore expected to reveal closely related features. For the singlet superconducting gaps, we use Ga's value of $|\Delta_{S,Ga}(0)| = 1.358$ meV as a reference and rescale all others according to Tab. S1, whereas we put exaggeratedly large triplet gaps—nearly four times as large—into our simulations in order to resolve clear ramifications of triplet pairings. Along the transverse direction, we include $W = 500$ lattice sites. Although changing W does not significantly impact the outcomes, using rather large numbers is reasonable to minimize unphysical numerical fluctuations in the generated DOS data.

IV. ROLE OF PURELY FERROMAGNETIC PROXIMITY EFFECTS

We argued in the main text that the rich conductance variations, appearing as the Ni–Ga thickness ratio continues to increase, signify superconducting triplet pairings around the Ni/Ga interface. To exclude that similar conductance anomalies might simply be caused by the pure ferromagnetic proximity effects that are additionally expected following our polarized-neutron reflectometry analyses (see Sec. V), we assume that the Ni interlayer furthermore induces the nonzero ferromagnetic exchange gap $\Delta_{XC,Ga}$ in Ga's proximity region (i.e., at all lattice sites indicated by L'_{Ga}), while the afore-

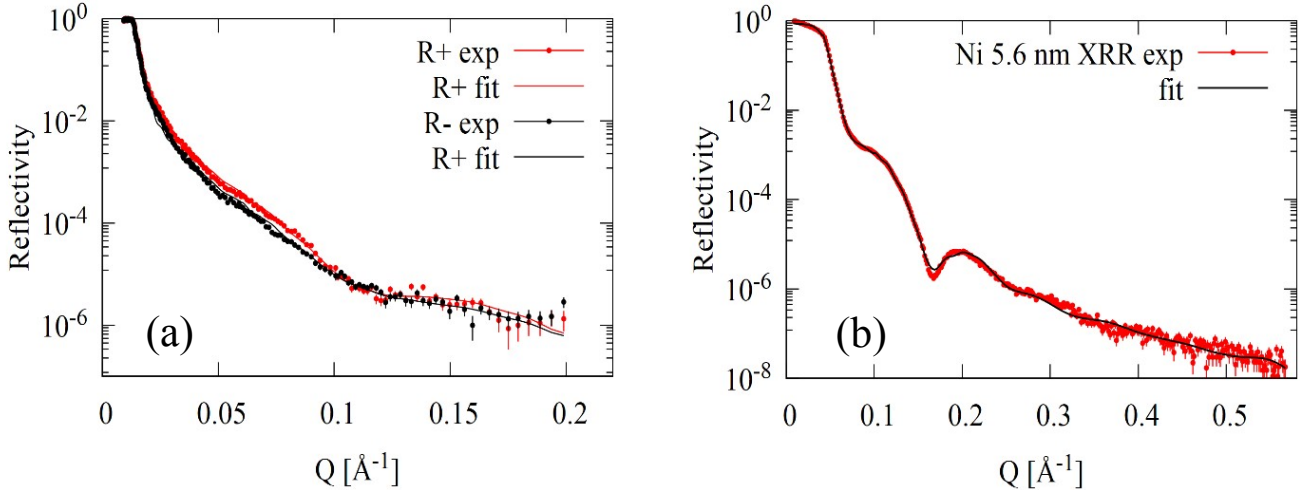


FIG. S6. Polarized-neutron reflectometry (PNR) and X-ray reflectometry (XRR) results for Ni (5.6 nm)/Ga (25 nm) bilayer. (a) Experimental reflectivity as a function of wave vector transfer Q for spin-up (R^+) and spin-down (R^-) neutron-spin states measured in 1 kOe after a zero-field cooling to 5 K. (b) Complementary X-ray reflectometry (XRR) data has been used to verify the films' depth morphology. From the fit to the PNR and XRR, we deduce that the Ni (5, 6 nm)/Ga (25 nm) interface is sharp with a roughness of 0.5 nm. The Ga layer's density is not uniform and consists of two roughly 6 nm and 19 nm thick sublayers (see also Fig. 4 in the main text).

mentioned triplet pairings are simultaneously no longer there. The tunneling DOS, numerically evaluated from KWANT for that case and shown in Fig. S4, suggests that even unrealistically great ferromagnetic proximity effects alone—raising proximity-induced gaps that are larger than Ni's actual exchange gap—are not enough to recover the experimentally observed features. The latter succeeds only if we allow for interfacial triplet pairings at the Ni/Ga boundary, as claimed in the main text. Anyhow, ferromagnetic proximity effects may strengthen the conductance peak at zero bias voltage, which becomes also evident in the experimental data and remains only barely visible when considering interfacial triplet pairings alone. Therefore, we conclude that we are probably concerned with a superposition of both effects in the experiment—triplet correlations around the Ni/Ga interface and (at least weak) ferromagnetic proximity inside the Ga electrode—which could also provide another reasonable explanation for the deviations between our theoretical toy model and the experimental results.

V. POLARIZED-NEUTRON REFLECTOMETRY

To better understand the Ni/Ga interfacial interaction, and to directly explore the depth profile of the magnetism at the interface, we employ a depth-sensitive polarized-neutron reflectometry (PNR) technique. Being electrically neutral, spin-polarized neutrons penetrate the entire multilayer structures, and probe magnetic and structural composition of the films through the buried interfaces down to the substrate [S13]. The PNR experiments were performed on the Magnetism Reflectometer at the Spallation Neutron Source at Oak Ridge National Laboratory [S14]. A neutron beam with a wavelength

band of 2.6–8.6 \AA and with a high polarization of 98.5% to 99% was used. After a zero-field cooling (ZFC), the measurements were performed at temperatures of 15 K and 5 K with an applied external magnetic field using a Bruker electromagnet with a maximum in-plane field up to 0.1 T. Using the time-of-flight method, a collimated polychromatic beam of polarized neutrons with the wavelength band $\Delta\lambda$ impinges on the film at a grazing incidence angle θ , where it interacts with atomic nuclei and the spins of unpaired electrons. The reflected intensity is measured as a function of wave vector transfer, $Q = 4\pi \sin \theta / \lambda$, for the two neutron polarizations R^+ and R^- , indicating a neutron spin parallel (+) or antiparallel (–) to the direction of the external field H_{ext} . To separate the nuclear from the magnetic scattering, the data is presented in terms of the spin-asymmetry ratio $SA = (R^+ - R^-) / (R^+ + R^-)$, as depicted in Fig. S5, as well as in Figs. 4(a) and 4(b) in the main text. A value of $SA = 0$ represents no magnetic moment in the system. The depth profiles of the *nuclear* and *magnetic scattering length densities* (*NSLD* and *MSLD*) correspond to the depth profiles of the chemical and in-plane magnetization vector distributions, respectively. The magnetization can then be calculated from the MSLD data using the relation $M(\text{emu/cc}) = \text{MSLD}(\text{\AA}^2) / (2.853 \times 10^{-9})$.

Complementary X-ray reflectometry (XRR) data has been used to verify the depth morphology of the films. The related experiments were carried out on the bilayers with Ga thickness fixed at 25 nm, while the Ni thickness varied (i.e., the Ni thickness was 0.8, 2.4, 4.0, and 5.6 nm). We investigated the bilayers' magnetization behavior above and below their critical temperature. The samples were analyzed under the same conditions as above, starting with ZFC down to 15 K and measuring at 1 kOe. Afterwards, the magnetic field was switched off, the sample got cooled to 5 K, and the

measurement repeated at 1 kOe. The samples with 5.6 nm and 4.0 nm thick Ni films showed clear magnetic signals [i.e., clear splittings between reflectivity for neutrons with spin-up (R^+) and spin-down (R^-)]. For samples containing 2.4 nm and 0.8 nm Ni regions, no measurable magnetization could be detected (see Fig. S5). The NSLD and MSLD depth profiles were obtained from a simultaneous fit to the PNR and XRR data, and finally plotted as functions of the depth from the surface; see Fig. S6 for, e.g., the sample with 5.6 nm thick Ni. PNR revealed a sharp interface between the Ni and Ga layers over the whole lateral size of the sample, with an average roughness of about 0.5 nm. The Ga layer's density was not uniform and consisted of two sublayers of 6 nm and 19 nm that could be attributed to the Ga growth given its high surface energy. Re-

markably, PNR showed 26 ± 5 emu/cc induced magnetization over roughly 6 nm in Ga, while the magnetization inside the Ni film was about 136 ± 5 emu/cc and uniform.

Spin-polarized tunneling studies investigating Al/Al₂O₃/Ni/Ga tunnel junctions through Meservey–Tedrow spectroscopy and with a Zeeman-split superconducting Al spin detector revealed a very similar magnetic behavior as a function of the Ni/Ga bilayers' Ni thickness—for Ni films thinner than 4 nm, it was hard to detect any spin polarization P (could be as small as 0.1%), whereas P could be clearly measured for 4 nm and larger Ni thicknesses—, being fully consistent with our PNR observations. The tunneling measurements were performed at 0.4 K and with an applied in-plane magnetic field of 3.3 T.

-
- [S1] M. Octavio, M. Tinkham, G. E. Blonder, and T. M. Klapwijk, Phys. Rev. B **27**, 6739 (1983).
 [S2] K. Flensberg, J. Bindslev Hansen, and M. Octavio, Phys. Rev. B **38**, 8707 (1988).
 [S3] C. W. Groth, M. Wimmer, A. R. Akhmerov, and X. Waintal, New J. Phys. **16**, 063065 (2014).
 [S4] P. M. Tedrow and R. Meservey, Phys. Rev. Lett. **26**, 192 (1971).
 [S5] P. M. Tedrow and R. Meservey, Phys. Rev. B **7**, 318 (1973).
 [S6] R. Meservey and P. M. Tedrow, Phys. Rep. **238**, 173 (1994).
 [S7] G. B. Arnold, J. Low Temp. Phys. **59**, 143 (1985).
 [S8] G. B. Arnold, J. Low Temp. Phys. **68**, 1 (1987).
 [S9] A. F. Andreev, Zh. Eksp. Teor. Fiz. **46**, 1823 (1964); J. Exp. Theor. Phys. **19**, 1228 (1964).
 [S10] Y. M. Blanter and F. W. J. Hekking, Phys. Rev. B **69**, 024525 (2004).
 [S11] J. M. Rowell and W. L. Feldmann, Phys. Rev. **172**, 393 (1968).
 [S12] M. Kuhlmann, U. Zimmermann, D. Dikin, S. Abens, K. Keck, and V. M. Dmitriev, Z. Phys. B **96**, 13 (1994).
 [S13] V. Lauter-Pasyuk, Collect. Soc. Fr. Neutron **7**, s221 (2007).
 [S14] V. Lauter-Pasyuk, H. J. Lauter, V. L. Aksenov, E. I. Kornilov, A. V. Petrenko, and P. Leiderer, Physica B **248**, 166 (1998).